In Situ RF Current Assessment for Array Transmission and Optimization

Adam C. Goad[®], Graduate Student Member, IEEE, Charles Baylis[®], Senior Member, IEEE, Trevor Van Hoosier, Graduate Student Member, IEEE, Austin Egbert[®], Member, IEEE, and Robert J. Marks[®], II, Life Fellow, IEEE

Abstract—In the increasingly congested wireless spectrum, phased-array transmitters can be used to provide spatial diversity as an additional measure of coexistence. Reconfigurable matching networks placed between the power amplifier device and the antenna can allow the amplifiers in the transmitter elements to maximize output power while maintaining the desired beam fidelity. A challenge with the use of reconfigurable matching networks in array transmitters is that they alter the system calibration. This article provides measurement validation of an in situ measurement approach to assess antenna input current using a dual-directional coupler placed in an array element. Measurement validation was performed using a two-port vector network analyzer (VNA) with a load—pull tuner emulating changing antenna impedance. This approach is expected to ease the process of maintaining the pattern and is expected to ease issues stemming from changing array calibration with reconfigurable array element circuits.

Index Terms—Amplifier, array calibration, coupler, network analysis, phased-array reconfigurable circuit.

I. INTRODUCTION

N THE increasingly congested wireless spectrum, spectrum-use systems benefit from the ability to adapt to their surroundings and reconfigure to optimize performance in available spectral and spatial channels. In transmitter power amplifiers, an impedance tuner placed between the power amplifier device and antenna can provide on-the-fly impedance matching to maximize output power (and corresponding transmission range) or efficiency while also minimizing nonlinearities that distort the spectrum and array pattern [1], [2], [3]. This real-time tunable behavior enables improved performance over wider bandwidths than is possible with a static transmitter design [4]. When a reconfigurable impedance tuner is placed in an element of a transmitter array, reconfiguring the impedance tuner can cause the magnitude

Manuscript received 2 March 2023; revised 19 May 2023 and 26 June 2023; accepted 30 June 2023. Date of publication 7 August 2023; date of current version 5 December 2023. This work was supported in part by the U.S. National Science Foundation under Grant 2030243. This paper is an expanded version from the IEEE International Symposium on Phased Array Systems and Technology, Waltham, MA USA, October 11–October 14, 2022 [DOI: 10.1109/PAST49659.2022.9975003]. (Corresponding author: Charles Baylis.)

The authors are with the Department of Electrical and Computer Engineering, Baylor University, Waco, TX 76798 USA (e-mail: Charles_Baylis@baylor.edu).

Color versions of one or more figures in this article are available at https://doi.org/10.1109/TMTT.2023.3298193.

Digital Object Identifier 10.1109/TMTT.2023.3298193

and phase of the element's transmission to change. If the impedances in different elements are tuned differently, this can alter the array pattern [5]. Because the surface current of the antenna determines the array pattern, it is desirable to monitor the antenna input current during impedance tuning to assess the effects of the tuning on the array transmission pattern. Our recent conference paper [6] proposes a method of measuring the current in antennas and provided simulation validation. In this extended version of the conference paper, we provide measurement validation of this approach (whereas the conference paper provided only initial simulation validation) and expand the theory initially presented in the conference paper to include nonideal measurement terminations. In addition, the simulation validation is extended to include nonideal measurement-port terminations.

Typical array transmitter calibration techniques assess the traveling-wave voltage magnitude and phase transmission parameters of each element using S-parameter (or equivalent) approaches. Calibration allows transmitter magnitude and phase offsets to be adjusted and allows receiver signal processing to be changed to ensure proper detection of the signal. If an uncorrected phase error exists, it can result in poor radar detection in radar arrays, as recognized by Flament et al. [7]. Pohlmann et al. [8] described a Bayesian algorithm that employs the Cramer-Rao bound if in an environment with unknown propagation parameters. Peccarelli and Fulton [9] described how mutual coupling can be used with nonlinear equalization to perform calibration through sensing intermodulation products. Takahashi et al. [10] performed an electric field measurement in space for calibration. Sippel et al. [11] described a near-field measurement of a known signal, transmitted by a beacon, to provide corrections for mutual coupling and multipath. Nicolas [12] demonstrated calibration performed using a mobile transmitter near the array surface, and Salazar et al. [13] described a calibration approach using an unmanned aerial system (UAS), flown near the array with an RF probe, to measure antenna patterns. Srinivas and Bliss [14] showed that aircraft arrays can suffer calibration issues from fuselage deformation and provided a calibration method using in situ sources and signals of opportunity. Lebron et al. [15] demonstrated self-calibration with arbitrary amplitude and phase. Fulton et al. [16] compared and categorized different array calibration approaches. In most array calibrations, external equipment or measurements are required.

0018-9480 © 2023 IEEE. Personal use is permitted, but republication/redistribution requires IEEE permission. See https://www.ieee.org/publications/rights/index.html for more information.

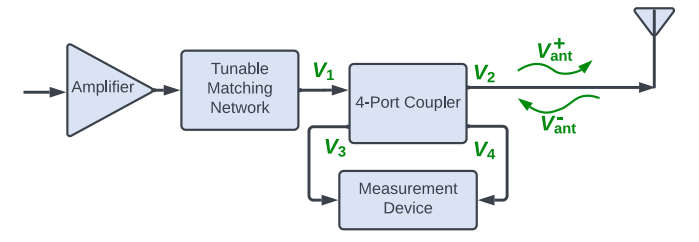


Fig. 1. In situ measurement setup with tunable matching network on a single element

Some array calibration techniques are achieved or maintained through the use of internal calibration networks. Aumann et al. [17] proposed the first mutual-coupling calibration method (MCCM) to improve the calibration of air and space flight systems. Bekers et al. [18] presented a method for using an MCCM that is robust to noise and module failure. Agrawal and Jablon [19] proposed adding passive receive elements into an array to be used for in field calibration. Fulton and Chappell [20] described several element-wise calibration techniques that can be used to assist with maintaining calibration over time for digital phased arrays. Lebron et al. [15] compared initial calibration against an in situ MCCM technique that provides greater accuracy and the ability to assist in element failure diagnosis. These methods have a common goal of determining drift from the initial calibration; they are not designed to handle the drastic changes in transmission characteristic that results from adaptively changing power, frequency, and load impedance.

While RF current measurements are difficult [21], [22], voltage measurements are simpler to perform. We present and include measurement validation of an approach to use two in situ voltage measurements to calculate the total current present at the input to the antenna of each individual array element. With these real-time current measurements, array calibration is greatly simplified since the antenna excitation can be known through changes in transmission characteristics, such as those induced by an impedance tuner, or varying mutual coupling environments.

II. METHODS

Fig. 1 shows a block diagram of how a four-port coupler can be used to assess the current incident on an antenna. This approach is an application of reflectometry techniques and provides a means for assessing antenna input current in real time. The following equations are derived in [6] to show how to calculate the antenna current:

$$I_{\text{ant}} = \frac{V_{\text{ant}}^+ - V_{\text{ant}}^-}{Z_0} \tag{1}$$

$$V_{\text{ant}}^{-} = \frac{V_4^{-} - \frac{S_{41}}{S_{31}} V_3^{-}}{S_{42} - \frac{S_{41}S_{32}}{S_{42}}}$$
 (2)

$$V_{\text{ant}}^{+} = \frac{S_{21}}{S_{31}} V_{3}^{-} + \left(S_{22} - \frac{S_{21} S_{32}}{S_{31}} \right) \frac{V_{4}^{-} - \frac{S_{41}}{S_{31}} V_{3}^{-}}{S_{42} - \frac{S_{41} S_{32}}{S_{31}}}.$$
 (3)

Fig. 1 shows the port voltages of the coupler (V_1, V_2, V_3, V_4) . Each port voltage (e.g., V_1) can be decomposed into a voltage traveling entering the port (V_1^+)

and a voltage wave leaving the port (V_1^-) , with respect to the reference impedance Z_0 . Fig. 1 also shows the traveling-wave voltages entering and leaving the antenna (V_{ant}^+) and V_{ant}^- , with respect to Z_0 .

While (1) stands without assumptions, (2) and (3) are only valid if $V_3^+ = V_4^+ = 0$, a condition assumed in the initial derivation of [6]. This requires that perfect, nonreflecting loads be connected to ports 3 and 4 of the coupler, which may not be a valid assumption depending on the measurement equipment used. As such, the exact assessment of $V_{\rm ant}^+$ and $V_{\rm ant}^-$ requires that these assumptions can be removed. The following equations generically define the waves leaving the ports $(V_1^-, V_2^-, V_3^-, V_4^-)$ in terms of the waves entering the ports $(V_1^+, V_2^+, V_3^+, V_4^+)$

$$V_1^- = S_{11}V_1^+ + S_{12}V_2^+ + S_{13}V_3^+ + S_{14}V_4^+ \tag{4}$$

$$V_2^- = S_{21}V_1^+ + S_{22}V_2^+ + S_{23}V_3^+ + S_{24}V_4^+$$
 (5)

$$V_3^- = S_{31}V_1^+ + S_{32}V_2^+ + S_{33}V_3^+ + S_{34}V_4^+$$
 (6)

$$V_4^- = S_{41}V_1^+ + S_{42}V_2^+ + S_{43}V_3^+ + S_{44}V_4^+.$$
 (7)

In addition, if the loads on ports 3 and 4 possess known reflection coefficients Γ_{L3} and Γ_{L4} , respectively, then

$$V_3^+ = \Gamma_{L3} V_3^- \tag{8}$$

and

$$V_4^+ = \Gamma_{I,4} V_4^-. \tag{9}$$

Solving (6) for V_1^+ and using (8) and (9) gives

$$V_1^+ = \frac{1}{S_{31}} \left(V_3^- - S_{32} V_2^+ - S_{33} \Gamma_{L3} V_3^- - S_{34} \Gamma_{L4} V_4^- \right). \tag{10}$$

Substituting (10) into (7), including use of (8) and (9), and solving for V_2^+ gives

$$V_{\text{ant}}^{-} = V_{2}^{+} = \frac{V_{3}^{-} \left(-\frac{S_{41}}{S_{31}} + \frac{S_{41}S_{33}}{S_{31}} \Gamma_{L3} - S_{43}\Gamma_{L3} \right)}{-\frac{S_{41}S_{32}}{S_{31}} + S_{42}} + \frac{V_{4}^{-} \left(\frac{S_{41}S_{34}}{S_{31}} \Gamma_{L4} - S_{44}\Gamma_{L4} + 1 \right)}{-\frac{S_{41}S_{32}}{C_{5}} + S_{42}}.$$
 (11)

Substituting (10) into (5) gives

$$V_{2}^{-} = V_{\text{ant}}^{+} = V_{2}^{+} \left(-\frac{S_{21}S_{32}}{S_{31}} + S_{22} \right)$$

$$+ V_{3}^{-} \left(\frac{S_{21}}{S_{31}} - \frac{S_{21}S_{33}}{S_{31}} \Gamma_{L3} + S_{23}\Gamma_{L3} \right)$$

$$+ V_{4}^{-} \left(-\frac{S_{21}S_{34}}{S_{31}} \Gamma_{L4} + S_{24}\Gamma_{L4} \right).$$
 (12)

Substituting (11) into (12) gives

$$V_{\text{ant}}^{+} = V_{2}^{-}$$

$$= V_{3}^{-} \left[\frac{\frac{-S_{21}S_{32}}{S_{31}} + S_{22}}{\frac{-S_{41}S_{32}}{S_{31}} + S_{42}} \left(-\frac{S_{41}}{S_{31}} + \frac{S_{41}S_{33}}{S_{31}} \Gamma_{L3} - S_{43}\Gamma_{L3} \right) + \frac{S_{21}}{S_{31}} - \frac{S_{21}S_{33}}{S_{31}} \Gamma_{L3} + S_{23}\Gamma_{L3} \right]$$

$$+V_{4}^{-} \left[\frac{\frac{-S_{21}S_{32}}{S_{31}} + S_{22}}{\frac{-S_{41}S_{32}}{S_{31}} + S_{42}} \left(\frac{S_{41}S_{34}}{S_{31}} \Gamma_{L4} - S_{44}\Gamma_{L4} + 1 \right) + \left(-\frac{S_{21}S_{34}}{S_{31}} \Gamma_{L4} + S_{24}\Gamma_{L4} \right) \right].$$
(13)

Finally, the next step is to substitute $V_3^- = V_3/(1 + \Gamma_{L3})$ and $V_4^- = V_4/(1 + \Gamma_{L4})$ into (11) and (13) to obtain expressions for $V_{\rm ant}^-$ and $V_{\rm ant}^+$ as follows:

$$V_{\text{ant}}^{-} = \frac{\frac{V_3}{1+\Gamma_{L3}} \left(-\frac{S_{41}}{S_{31}} + \frac{S_{41}S_{33}}{S_{31}} \Gamma_{L3} - S_{43}\Gamma_{L3} \right)}{-\frac{S_{41}S_{32}}{S_{31}} + S_{42}} + \frac{\frac{V_4}{1+\Gamma_{L4}} \left(\frac{S_{41}S_{34}}{S_{31}} \Gamma_{L4} - S_{44}\Gamma_{L4} + 1 \right)}{-\frac{S_{41}S_{32}}{S_{31}} + S_{42}}$$

$$V_{\text{ant}}^{+} = \frac{V_3}{1+\Gamma_{L3}} \left[\frac{\frac{-S_{21}S_{32}}{S_{31}} + S_{22}}{\frac{-S_{41}S_{32}}{S_{31}} + S_{42}} \left(-\frac{S_{41}}{S_{31}} + \frac{S_{41}S_{33}}{S_{31}} \Gamma_{L3} - S_{43}\Gamma_{L3} \right) + \frac{S_{21}}{S_{31}} - \frac{S_{21}S_{32}}{S_{31}} + S_{42} \left(\frac{S_{41}S_{34}}{S_{31}} \Gamma_{L3} + S_{23}\Gamma_{L3} \right) + \frac{V_4}{1+\Gamma_{L4}} \left[\frac{\frac{-S_{21}S_{32}}{S_{31}} + S_{22}}{\frac{-S_{41}S_{32}}{S_{31}} + S_{42}} \left(\frac{S_{41}S_{34}}{S_{31}} \Gamma_{L4} - S_{44}\Gamma_{L4} + 1 \right) + \left(-\frac{S_{21}S_{34}}{S_{31}} \Gamma_{L4} + S_{24}\Gamma_{L4} \right) \right].$$

$$(14)$$

This gives $V_{\rm ant}^-$ and $V_{\rm ant}^+$ in terms of the total measured voltages V_3 and V_4 . Unlike (2) and (3), (14) and (15) use total voltage measurements and account for the reflection from each port of the measurement device. This expands the measurement techniques that can be used to implement this method. For example, a software-defined radio platform (which measures total voltage and does not separate incident and reflected voltage waves) could be used in conjunction with an actual array platform to assess the total voltages V_3 and V_4 , calculating $V_{\rm ant}^-$ and $V_{\rm ant}^+$ using (14) and (15), respectively, and using these calculated voltages to assess the antenna current through (1).

In present state-of-the-art techniques, array calibration includes the characterization of the full transmit amplifier chain and often the antennas, channel, and receiver chain. However, the calibration is invalidated as the transmitter reconfigurable matching network is reconfigured. As such, the use of traditional array calibration techniques in a situation involving a reconfigurable matching network would require a precalibration for each possible matching network setting. This is an involved task, due to the vast number of possible tuning configurations of the full array. Using direct monitoring of the antenna current eliminates the need for these precalibrations and, if the antenna pattern is known, allows monitoring of the array pattern in real time. This current monitoring method requires characterization only of the passive four-port coupler and antenna.

III. SIMULATION VALIDATION

As described in [6], this approach was validated using simulations from Keysight's advanced design system (ADS). Fig. 2 shows a simple validation of this method (from [5])

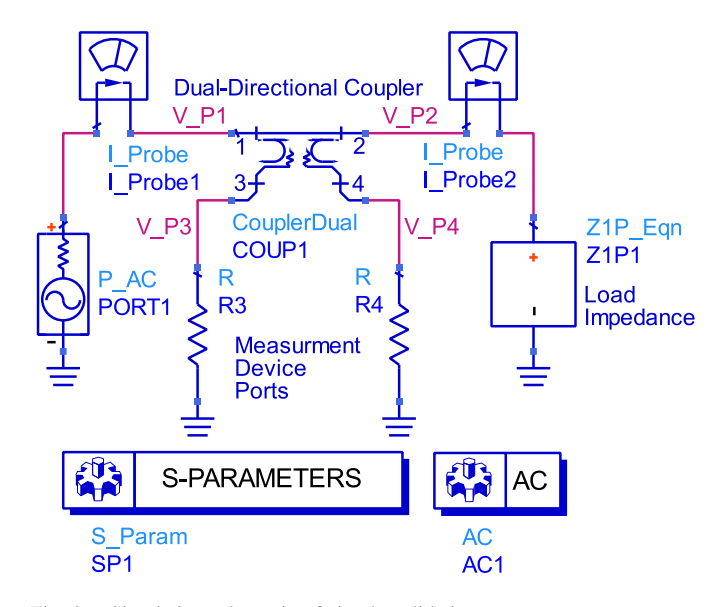


Fig. 2. Simulation schematic of simple validation.

TABLE I
SIMPLE SIMULATION VALIDATION TEST RESULTS, REPRINTED FROM [5]

| # | $Z_s(\Omega)$ | $Z_L(\Omega)$ | $V_3(V)$ | $V_4(V)$ | $I_{meas}(A)$ | $I_{calc}(A)$ |
|---|---------------|---------------|------------------|--------------------|-------------------|-------------------|
| 1 | 50 | 50 | 5.62 <u>/90°</u> | 1.00 <u>/90°</u> | 0.54 <u>/0°</u> | 0.54 <u>/0°</u> |
| 2 | 50 | 5 | 5.66 <u>/96°</u> | 3.71 <u>/-74°</u> | 0.89 <u>/0°</u> | 0.89 <u>/0°</u> |
| 3 | 50 | 5+j15 | 5.98 <u>/95°</u> | 3.29 <u>/-105°</u> | 0.87 <u>/-12°</u> | 0.87 <u>/-12°</u> |
| 4 | 15 | 50 | 4.43 <u>/90°</u> | 0.787 <u>/0°</u> | 0.43 <u>/0°</u> | 0.43 <u>/0°</u> |
| 5 | 15+j8 | 50 | 5.58 <u>/75°</u> | 0.783 <u>/-6°</u> | 0.43 <u>/-6°</u> | 0.43 <u>/-6°</u> |

using a model of an ideal dual-directional coupler. Table I shows the results of the simulation validation. Using ADS, V_3^- and V_4^- were assessed, and using (2) and (3) with (1) was used to calculate I_{calc} . The "ground truth" for comparison, I_{meas} , is assessed through the ADS current probe tool [element "I_Probe2" in Fig. 2 (simulation schematic)]. Table I shows the results for this test with various source and load impedances using (2) and (3) with ideal $50-\Omega$ loads acting as the measurement device termination. These results demonstrate complete agreement between the simulated current and the result produced through the previously published method [5] (verified to floating-point precision). Because the simulator simply implements the same circuit theory that has been laid out in our equations, it is expected that, given this approach is theoretically validated, and the simulator would use the voltages to accurately calculate the antenna current.

To validate the more general case derived in Section II [specifically (14) and (15)], the schematic in Fig. 3 was used. This test used measured S-parameters of a coupler and allowed the ability to change not only the source and load impedances but also the impedance of the measurement device(s) on the other two ports.

Several different impedances were connected to ports 3 and 4 of the coupler to test this approach. The results of some of these tests are shown in Table II. The currents $I_{\rm calc}$ shown in Table II, calculated using (1), (14), and (15), match the $I_{\rm meas}$ results from the ADS current probe in all cases to floating-point precision. This simulation demonstrates the applicability of our method to imperfect

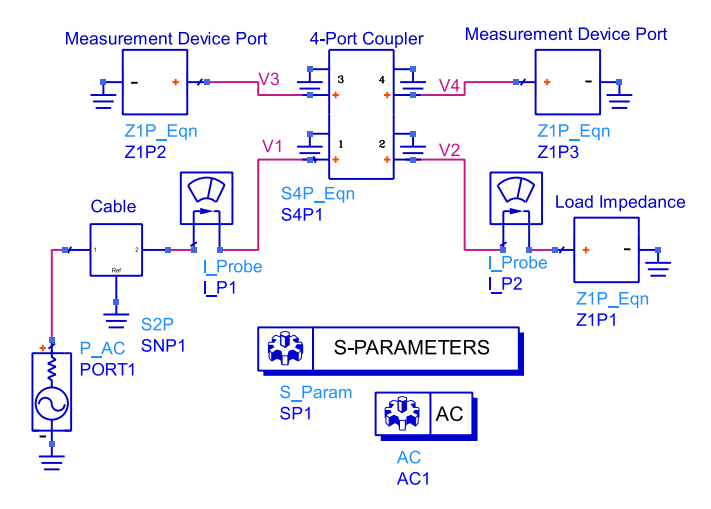


Fig. 3. ADS schematic of advanced simulation validation.

TABLE II
ADVANCED SIMULATION VALIDATION TEST RESULTS

| # | $Z_s(\Omega)$ | $Z_L(\Omega)$ | $Z_3(\Omega)$ | $Z_4(\Omega)$ | $I_{meas}(A)$ | $I_{calc}(A)$ |
|---|----------------|---------------|---------------|---------------|----------------------|----------------------|
| 1 | 50 | 50 | 50 | 50 | 0.54 <u>/-59.30°</u> | 0.54 <u>/-59.30°</u> |
| 2 | 50 | 5 | 15 | 35 | 0.98 <u>/-59.69°</u> | 0.98 <u>/-59.69°</u> |
| 3 | 50 | 5+j15 | 15+j25 | 35+j5 | 0.94 <u>/-74.96°</u> | 0.94 <u>/-74.96°</u> |
| 4 | 15 | 50 | 15+j25 | 155 | 0.45 <u>/-59.30°</u> | 0.45 <u>/-59.30°</u> |
| 5 | 15+ <i>j</i> 8 | 50 | 250 | 155+j30 | 0.45 <u>/-66.29°</u> | 0.45 <u>/-66.29°</u> |

measurement equipment using the more complete calculations prescribed in (1), (14), and (15). As expected, the results correlate exactly in an environment free from measurement noise and repeatability issues.

IV. MEASUREMENT VALIDATION

In addition to simulation testing, we have validated the ability to assess the antenna currents with measured voltage waves. Fig. 4(a) shows a block diagram of the measurement setup. One port of a vector network analyzer (VNA) is used to generate an incident voltage wave V_1^+ to port 1 of the dual-directional coupler, and a second VNA port was used to sequentially measure the traveling-wave voltages V_3^- and V_4^- based on the transmission measurement of the VNA (giving S_{31} and S_{41}). These measurements were performed sequentially, as only a two-port network analyzer was available for the measurement. The port not terminated in the second port of the network analyzer was terminated in a 50- Ω load, with a 6-dB attenuator further removing unwanted reflections. A photograph of the measurement setup is shown in Fig. 4(b). Because the network analyzer is capable of assessing traveling-wave voltages, (11) and (13) were used with the VNA-measured data to calculate $V_{\rm ant}^-$ and $V_{\rm ant}^+$ for use in (1).

A Keysight Technologies E5071C ENA network analyzer was used as the VNA. A Krytar 501004020 dual-directional coupler was used as the four-port coupler, and a Maury Microwave MT982B load—pull tuner was used to emulate changing antenna reflection coefficients $\Gamma_{\rm ant}$. The S-parameters of each component and cable assemblage were precharacterized using the E5071C VNA, and correction was performed

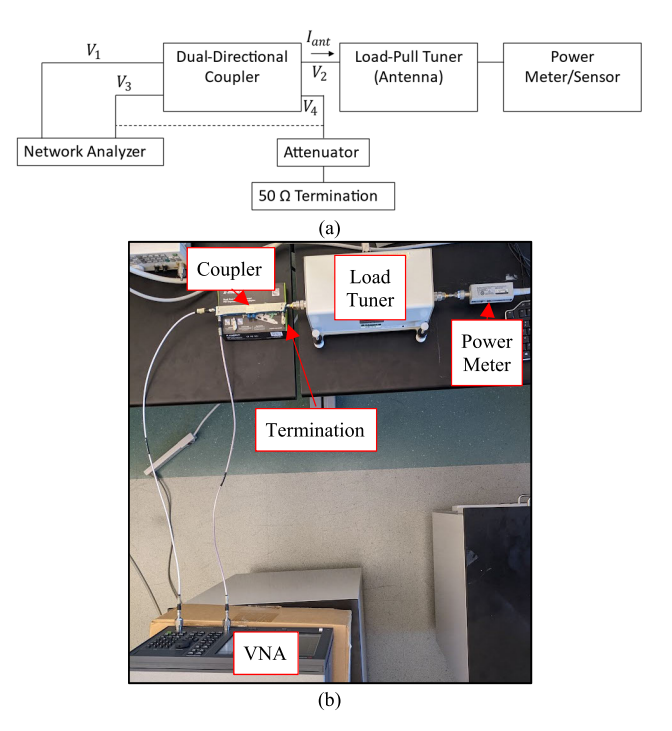


Fig. 4. Measurement validation bench (a) block diagram and (b) photograph. The dashed line in (a) indicates that the loads presented to ports 3 and 4 of the coupler are swapped to allow sequential measurement of both ports.

Load Reflection Coefficients

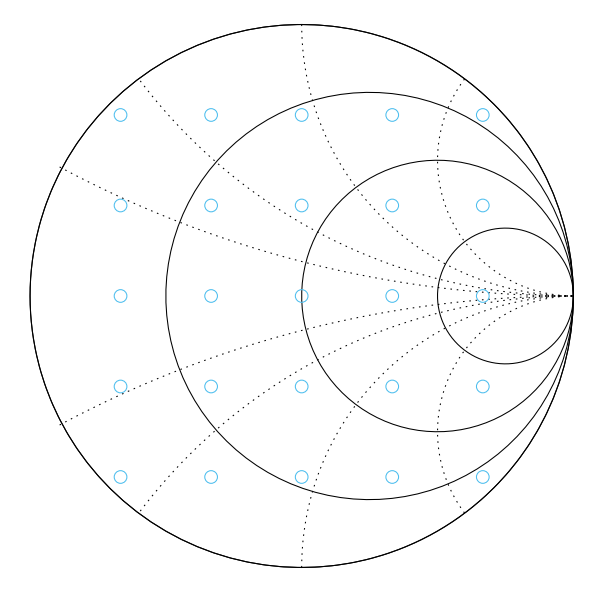


Fig. 5. Emulated values of antenna reflection coefficient Γ_{ant} using the load—pull tuner.

based on these characterizations in the measurement. In practice, such precorrections would be performed before deployment of the array.

Because of the VNA calibration, along with the termination of the non-VNA connected port to the 6-dB attenuator and $50-\Omega$ load used during its characterization, it was assumed $\Gamma_{L3} = \Gamma_{L4} = 0$ allowing use of (11) and (13).

Measurement validation was performed across different Γ_{ant} values (shown in Fig. 5), resulting in varying values of vector antenna current I_{ant} . For comparison, the calculation of current

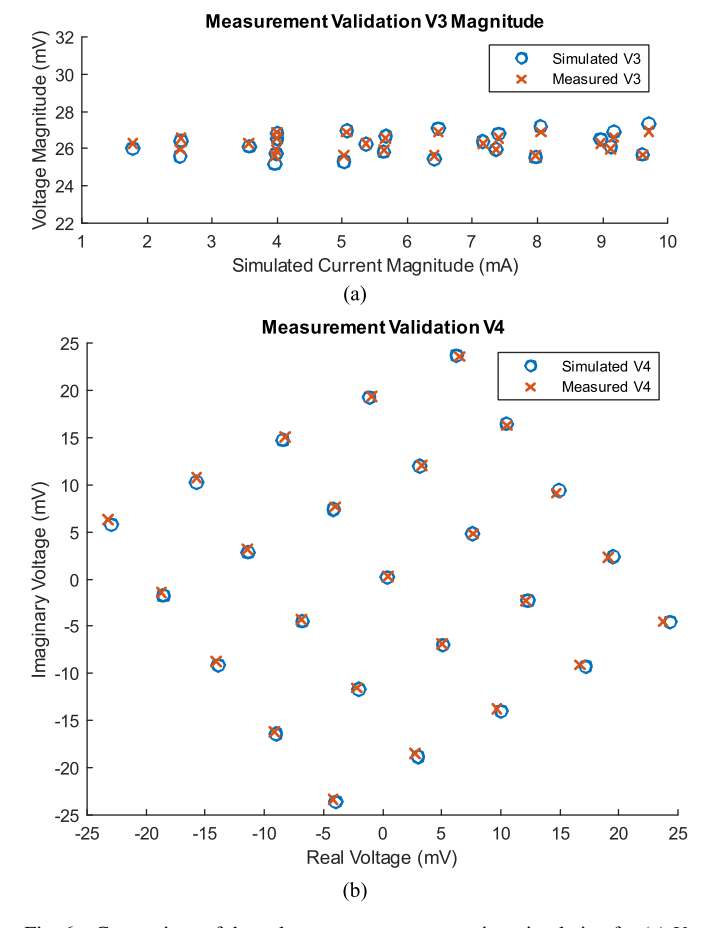


Fig. 6. Comparison of the voltage measurements against simulation for (a) V_3 and (b) V_4 . V_3 is used as the zero phase reference; as such, only magnitude is shown.

for the same 25 points was performed in the ADS simulator for comparison. In both simulation and measurement, V_3 was chosen as the phase reference of zero degrees.

Fig. 6 compares the measured and simulated voltages of both ports 3 and 4. When compared with the simulation results using the same input voltage and the characterized-network S-parameters, the magnitudes of V_3 have a maximum percent error of 1.72% and an average error magnitude of 179.49 μ V. The values for V_4 have a maximum percent error of 25.98%, but this occurs at the point where the load was set to 50 Ω , and the magnitude of V_4 is near zero. The actual voltage error magnitude is only 108.11 μ V. The average voltage error magnitude is 330.12 μ V.

Fig. 7 shows the view of the error vector magnitudes (EVMs) of V_3 and V_4 in terms of the difference between the measured and simulated of the voltages for the different current magnitudes caused by the differing $\Gamma_{\rm ant}$ values. Table III lists both voltage values for each point and provides the EVM values. The simulated and measured values appear nearly identical, with the largest EVM value of only $609.64~\mu V$.

The strong agreement between these simulations and measurements demonstrates accurate modeling of the test setup in the simulator. This means that it is expected that the measured and simulated values of $I_{\rm ant}$ are also expected to have good correspondence.

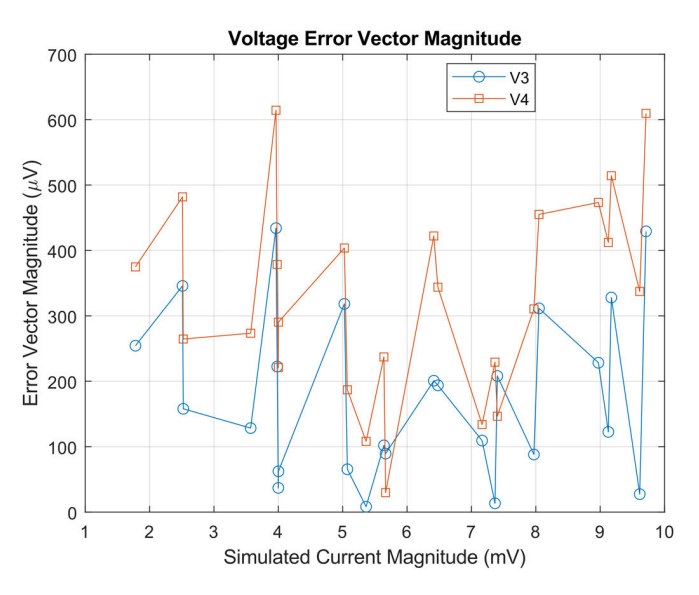


Fig. 7. EVM comparison of measured and simulated voltages.

TABLE III VOLTAGE VALUES AND ERROR

| # | Sim | $\operatorname{Sim} V_4(mV)$ | Meas | Meas $V_4(mV)$ | EVM | EVM |
|----|-----------|------------------------------|-----------|-----------------------|--------------|--------------|
| | $V_3(mV)$ | | $V_3(mV)$ | | $V_3(\mu V)$ | $V_4(\mu V)$ |
| 1 | 26.26 | 0.54 <u>/23.7°</u> | 26.26 | 0.51 <u>/30.3°</u> | 8.32 | 108.11 |
| 2 | 26.67 | 8.99 <u>/32.2°</u> | 26.58 | 9.02 <u>/32.1°</u> | 89.44 | 29.83 |
| 3 | 26.13 | 8.49 <u>/119.2°</u> | 26.26 | 8.65 <u>/117.7°</u> | 128.45 | 273.45 |
| 4 | 25.84 | 8.13 <u>/-146.6°</u> | 25.95 | 8.10 <u>/-148.3°</u> | 102.03 | 237.24 |
| 5 | 26.38 | 8.66 <u>/-53.8°</u> | 26.27 | 8.52 <u>/-53.9°</u> | 109.37 | 133.85 |
| 6 | 26.80 | 12.50 <u>/-10.5°</u> | 26.59 | 12.37 <u>/-10.8°</u> | 208.08 | 146.57 |
| 7 | 26.55 | 12.36 <u>/75.3°</u> | 26.58 | 12.52 <u>/74.6°</u> | 37.04 | 221.00 |
| 8 | 25.72 | 11.72 <u>/166.0°</u> | 25.94 | 11.90 <u>/164.4°</u> | 222.55 | 378.58 |
| 9 | 25.97 | 11.85 <u>/-99.7°</u> | 25.96 | 11.73 <u>/-100.7°</u> | 13.45 | 229.21 |
| 10 | 27.08 | 17.62 <u>/32.2°</u> | 26.89 | 17.30 <u>/31.8°</u> | 193.85 | 343.87 |
| 11 | 26.01 | 17.00 <u>/119.9°</u> | 26.27 | 17.12 <u>/118.7°</u> | 254.39 | 374.84 |
| 12 | 25.44 | 16.63 <u>/-146.7°</u> | 25.64 | 16.57 <u>/-148.1°</u> | 200.81 | 422.15 |
| 13 | 26.52 | 17.26 <u>/-54.4°</u> | 26.29 | 16.82 <u>/-55.0°</u> | 228.37 | 473.35 |
| 14 | 26.93 | 19.51 <u>/-28.4°</u> | 26.60 | 19.00 <u>/-28.6°</u> | 328.01 | 514.27 |
| 15 | 27.21 | 19.68 <u>/7.0°</u> | 26.90 | 19.22 <u>/6.9°</u> | 311.50 | 455.07 |
| 16 | 26.96 | 19.53 <u>/57.5°</u> | 26.90 | 19.39 <u>/57.2°</u> | 66.56 | 186.96 |
| 17 | 26.43 | 19.24 <u>/93.3°</u> | 26.59 | 19.36 <u>/92.6°</u> | 157.96 | 264.60 |
| 18 | 25.60 | 18.78 <u>/146.9°</u> | 25.95 | 19.05 <u>/145.7°</u> | 345.83 | 481.91 |
| 19 | 25.31 | 18.63 <u>/-174.6°</u> | 25.63 | 18.75 <u>/-175.8°</u> | 318.34 | 403.75 |
| 20 | 25.56 | 18.74 <u>/-118.8°</u> | 25.65 | 18.57 <u>/-119.6°</u> | 88.06 | 310.59 |
| 21 | 26.10 | 19.04 <u>/-81.0°</u> | 25.98 | 18.66 <u>/-81.4°</u> | 122.62 | 412.21 |
| 22 | 27.34 | 24.76 <u>/-10.6°</u> | 26.92 | 24.16 <u>/-10.8°</u> | 429.23 | 609.64 |
| 23 | 26.84 | 24.49 <u>/75.1°</u> | 26.91 | 24.47 <u>/74.5°</u> | 62.37 | 290.37 |
| 24 | 25.20 | 23.67 <u>/165.9°</u> | 25.63 | 24.05 <u>/164.8°</u> | 434.08 | 614.32 |
| 25 | 25.69 | 23.93 <u>/-99.6°</u> | 25.67 | 23.71 <u>/-100.2°</u> | 27.48 | 337.27 |

Fig. 8 compares the antenna current $I_{\rm ant}$, based on the measurement of V_3^- and V_4^- and use of (1), (11), and (13) with the current value assessed directly in simulation using the current probe tool. The measured current values have an average error magnitude of 66.87 μA and average percent error of 1.23%. The maximum current error magnitude was 187.93 μA , with a maximum percent error of 4.42% observed.

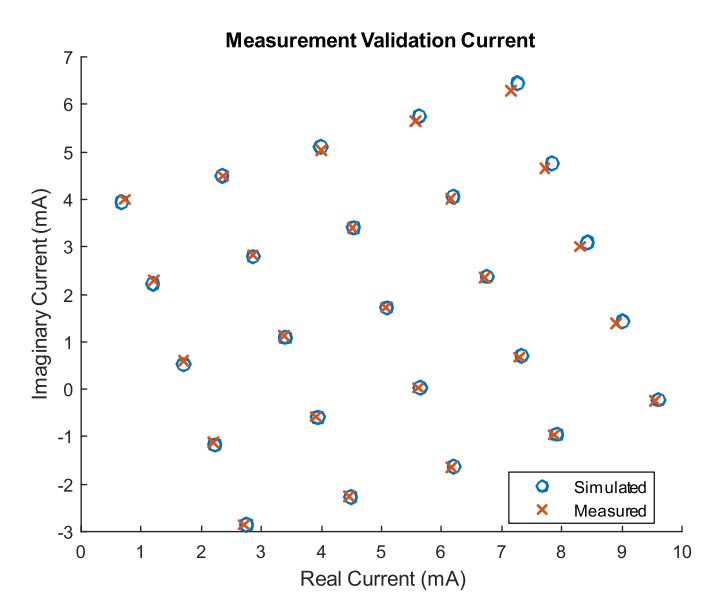


Fig. 8. Comparison of measured and simulated currents for all points on the complex plane.

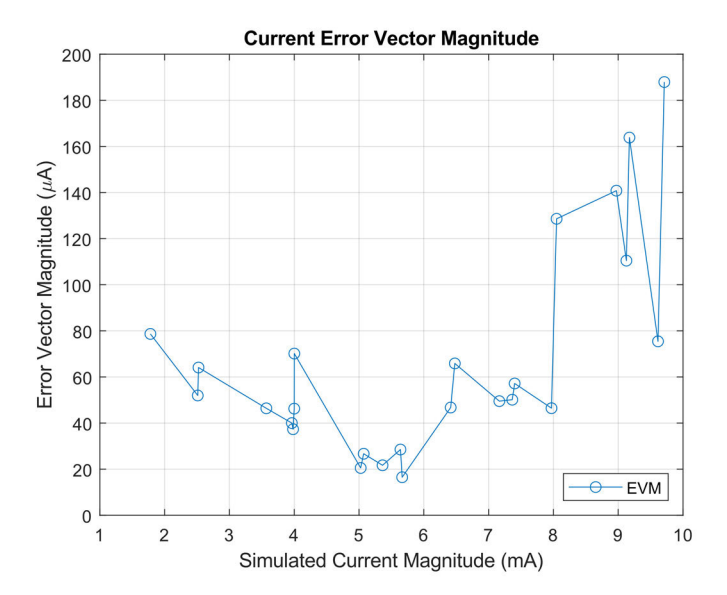


Fig. 9. Residual error vectors of measured and simulated current.

Fig. 9 shows the comparison between measurement and simulation in terms of the difference residuals. As expected, the EVM of the current generally increases for reflection coefficient values $\Gamma_{\rm ant}$ resulting in larger current magnitudes. However, the percent error is small for all of the reflection coefficients assessed. The maximum EVM in Fig. 9 relates to a percent error of only 1.93% (this is a 187- μ A EVM for a 9.71-mA measurement).

V. APPLICATION TO ARRAY CALIBRATION

To demonstrate the application of this method to array calibration, a simulation experiment was conducted using a four-element digital array. This simulation is performed in ADS and iteratively uses in situ monitoring of the current to adjust the input voltages to the power amplifiers. Because the approach measures the antenna currents and adjusts the

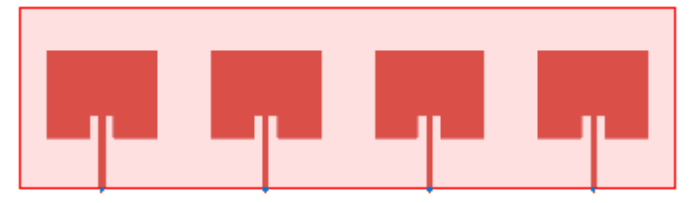


Fig. 10. Patch antenna array for electromagnetic simulation with the ADS Momentum Microwave simulator.

input voltages iteratively, it corrects for differences in the transconductance magnitude and phase between the elements, the nonlinear effects of the power amplifiers, and the mutual coupling between array elements.

A simulation was constructed to examine the effectiveness of this approach. Using the ADS Momentum Microwave simulator, a simple four-element linear microstrip patch antenna array was constructed. The construction of this array, as shown in the ADS Momentum Microwave electromagnetic simulator, is included in Fig. 10. These element antennas were arranged linearly in the magnetic field plane. Using a harmonic balance simulation, each element was excited using a voltage source with relative magnitude and phase values calculated for an array. A GaAs metal-semiconductor field-effect transistor (MESFET) model from Modelithics was used to simulate the nonlinear transistor in each element. The port current entering each antenna was calculated in the harmonic balance simulation, and these current values were used in Momentum Microwave electromagnetic simulations to determine the array pattern. The schematic for this simulation is shown in Fig. 11. The amplifier blocks contain the Modelithics nonlinear models and the amplifier matching networks. Inside the In situ Measurer block are the measured S-parameters of a dual-directional coupler, where the coupled ports are connected to impedance blocks that match the measured values of our measurement equipment.

To demonstrate the capability of the system to make on-the-fly corrections, the output matching network in each element was set to a different impedance value to replicate the effects of impedance tuning. To perform the calibration, the input voltage values and the output current values, found using in situ measurements, are used to calculate the transconductance of each element. The transconductances and the desired output element output currents ($i_{ideal,n}$) are then used to calculate new input voltage values using (16)–(18). The input weights for each iteration are determined by

$$w_{\text{in},n}(t) = \frac{i_{\text{ideal},n}}{G_n(t-1)}$$
(16)

where G_n is the transconductance of the nth element, which is calculated as

$$G_n(t) = \frac{i_{\text{out},n}(t)}{v_{\text{in }n}(t)}.$$
 (17)

The weights are then normalized to the maximum power level set by the user, P_{max} , to get input voltage values using

$$v_{\text{in},n}(t) = w_{\text{in},n}(t) \sqrt{\frac{2P_{\text{max}}Z_0}{\max_n(|w_{\text{in},n}(t)|)^2}}.$$
 (18)

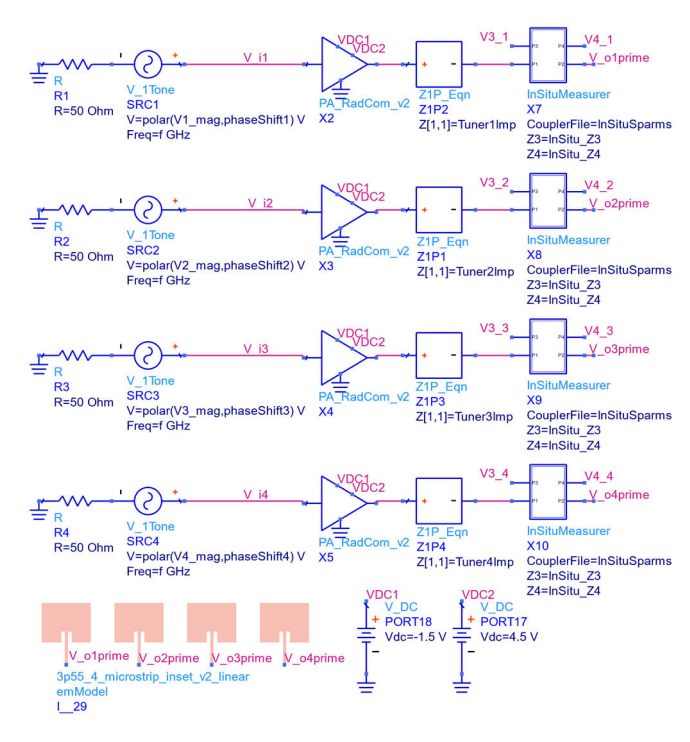


Fig. 11. ADS schematic used for array calibration with harmonic balance simulation.

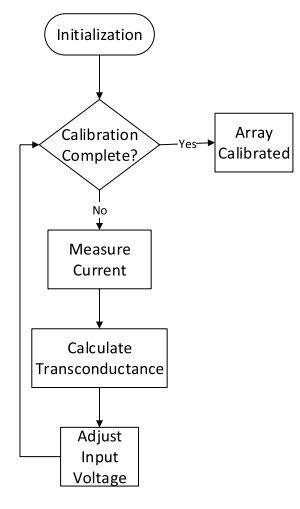


Fig. 12. Flowchart of array transmitter calibration process. In this work, calibration is complete after a set number of iterations is reached but a more sophisticated method of convergence testing could be applied.

This process is then repeated in an iterative manner, as shown in Fig. 12, until a desired number of iterations or level of performance is reached.

Fig. 13 shows the results of using this calibration with a simple four-element array transmit beam steered to 30° off broadside. To create a beam at this angle, each element must be excited with signals identical in magnitude and separated in phase by $kd \sin 30^{\circ}$, where k is the phase constant in radians per meter and d is the separation between the element antennas in meters (in this setup, $d = \lambda/2$, where λ is the wavelength in meters). Because $k = 2\pi/\lambda$, the element excitations are

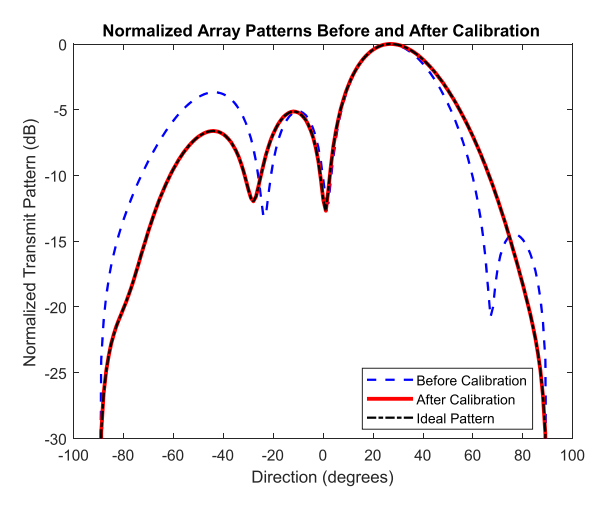


Fig. 13. Comparison of array transmission pattern before and after calibration, compared to an ideal transmission pattern with all plots normalized to the same maximum amplitude.

separated in phase by

$$kd \sin 30^{\circ} = \left(\frac{2\pi}{\lambda}\right) \left(\frac{\lambda}{2}\right) \sin\left(\frac{\pi}{6}\right) = \frac{\pi}{2} = 90^{\circ}.$$
 (19)

Before calibration, all elements were excited with the same magnitude and 90° relative phase shifts to produce the desired beam steering. This traditional input resulted in the distorted pattern shown with the blue dashed line in Fig. 13. The sidelobe at -45° is significantly overpronounced in the resulting pattern. The in situ measurement process is then used to perform an "on-the-fly" array calibration, correcting the input voltages based on the measured antenna currents. The resulting pattern, shown as the red solid trace in Fig. 13, is nearly identical to the ideal transmission pattern (blue dotted-dashed trace).

A numerical comparison between the ideal currents and the measured currents across the elements can be performed. Because the relative currents determine the array pattern, a normalized current can be calculated for each element relative to the mean current across all elements. This can be performed for the ideal element currents and the in situ measured element currents. The normalized ideal and measured current values, respectively, for the *n*th element of an *N* element array are given as follows:

$$i_{\text{ideal},n} = \frac{I_{\text{ideal},n}}{\left(\frac{\sum_{n=1}^{N} |I_{\text{ideal},n}|}{N}\right)}$$
(20)

$$i_{\text{meas},n} = \frac{I_{\text{meas},n}}{\left(\frac{\sum_{n=1}^{N} |I_{\text{meas},n}|}{N}\right)}.$$
 (21)

These normalized element current values can be used to calculate a percent error of each element's measured relative current value when compared to the element's ideal relative current value. For the *n*th element, the percent error is defined as follows:

$$E_n = \left| \frac{i_{\text{ideal},n} - i_{\text{meas},n}}{i_{\text{ideal},n}} \right| \times 100\%. \tag{22}$$

Before the calibration was performed, the percentage error values of up to 221.9% were observed for E_n . Following calibration using the in situ measurements, the maximum E_n was reduced to 6.5×10^{-7} % after 20 iterations of correction. The array pattern after calibration in Fig. 13 is right on top of the desired pattern trace, to the extent that the traces are nearly indistinguishable from each other. The actual speed of this number of iterations would likely be based on the measurement processing time of the in situ measurement device and the required computation time for the excitation adjustments, but 20 iterations seem reasonable for real-time implementation. The feasibility of this number of iterations should be examined in implementing this in a realistic system for measurements.

Simply put, the insertion of in situ current monitoring precludes the need for advance calibration and allows monitoring of actual current. Thus, it provides two specific benefits: 1) it removes the need for traditional array precalibration and 2) it corrects for changes or adjustments during operation, such as reconfiguration of impedance tuners and mutual coupling effects.

VI. CONCLUSION

A method of monitoring the current entering a phased-array antenna has been measurement validated using traveling-wave voltage measurements with a four-port dual-directional coupler. Furthermore, a measurement approach allowing the total voltage at the coupled ports has been derived and validated through extended simulation results. This approach is designed for in situ implementation in array transmitter elements and is expected to be especially useful when element transmission magnitude and phase are expected to vary in real time, such as when real-time impedance tuning is performed in the element, or mutual coupling changes antenna impedance (especially when mutual coupling varies from element to element). Very importantly, the ability to monitor the input current to the array antennas allows calculation of the array transmit pattern if the individual antenna patterns are predetermined. This removes the need for pre-calibration of the transmitter at all possible tuner settings. Further, this method may either replace or provide useful assistance to traditional array calibration for some applications. When implemented in an array setup, this approach is expected to enable the use and reconfiguration of tunable matching networks to optimize array performance with changing transmission characteristics in a dynamic environment. The theoretical, simulation, and measurement-based justification of the in situ monitoring approach presented in this article should allow practitioners to develop this for real-time use in an actual transmitter with confidence that it will provide accurate monitoring of the antenna currents.

ACKNOWLEDGMENT

The authors wish to thank Keysight Technologies for donation of the ADS software, Baylor University. They are grateful to Modelithics for the donation of software component model libraries to Baylor University under the Modelithics University Program. They are also grateful to Krytar for loan of the coupler used in these experimental validations.

REFERENCES

- J. Alcala-Medel et al., "Fast frequency-agile real-time optimization of high-power tuning network for cognitive radar applications," in *IEEE MTT-S Int. Microw. Symp. Dig.*, Boston, MA, USA, Jun. 2019, pp. 1466–1469.
- [2] M. Fellows, C. Baylis, L. Cohen, and R. J. M. Ii, "Real-time load impedance optimization for radar spectral mask compliance and power efficiency," *IEEE Trans. Aerosp. Electron. Syst.*, vol. 51, no. 1, pp. 591–599, Jan. 2015.
- [3] P. Rodriguez-Garcia, J. Sifri, C. Calabrese, A. Goad, C. Baylis, and R. J. Marks II, "Spurious beam suppression in dual-beam phased array transmission by impedance tuning," *IEEE Trans. Aerosp. Electron. Syst.*, vol. 58, no. 5, pp. 3932–3945, Oct. 2022.
- [4] J. Roessler et al., "Enhancing frequency-agile radar range over a broad operating bandwidth with reconfigurable transmitter amplifier matching networks," in *Proc. IEEE Radar Conf. (RadarConf)*, Atlanta, GA, USA, May 2021, pp. 1–5.
- [5] P. Rodriguez-Garcia, J. Sifri, C. Calabrese, C. Baylis, and R. J. Marks, "Range improvement in single-beam phased array radars by amplifier impedance tuning," in *Proc. IEEE Texas Symp. Wireless Microw. Circuits Syst. (WMCS)*, Waco, TX, USA, May 2021, pp. 1–6.
- [6] C. Baylis, A. Goad, T. Van Hoosier, A. Egbert, and R. J. Marks, "In-situ assessment of array antenna currents for real-time impedance tuning," in *Proc. IEEE Int. Symp. Phased Array Syst. Technol. (PAST)*, Waltham, MA, USA, Oct. 2022, pp. 1–4.
- [7] P. J. Flament et al., "In-situ calibration methods for phased array high frequency radars," in *Proc. Amer. Geophys. Union, Fall Meeting*, Dec. 2016.
- [8] R. Pöhlmann, S. Zhang, E. Staudinger, S. Caizzone, A. Dammann, and P. A. Hoeher, "Bayesian in-situ calibration of multiport antennas for DoA estimation: Theory and measurements," *IEEE Access*, vol. 10, pp. 37967–37983, 2022.
- [9] N. Peccarelli and C. Fulton, "A mutual coupling approach to digital pre-distortion and nonlinear equalization calibration for phased arrays," in *Proc. IEEE Int. Symp. Phased Array Syst. Technol.*, Waltham, MA, USA, Oct. 2019, pp. 1–8.
- [10] T. Takahashi, Y. Konishi, and I. Chiba, "A novel amplitude-only measurement method to determine element fields in phased arrays," *IEEE Trans. Antennas Propag.*, vol. 60, no. 7, pp. 3222–3230, Jul. 2012.
- [11] E. Sippel, M. Lipka, J. Gei
 ß, M. Hehn, and M. Vossiek, "In-situ calibration of antenna arrays within wireless locating systems," *IEEE Trans. Antennas Propag.*, vol. 68, no. 4, pp. 2832–2841, Apr. 2020.
- [12] J.-J. Nicolas, "Measurements of phased array antenna fields in situ: A few key aspects," in *Proc. IEEE Radar Conf.*, Rome, Italy, May 2008, pp. 1–6.
- [13] J. L. Salazar, A. Umeyama, S. Duthoit, and C. Fulton, "UAS-based antenna pattern measurements and radar characterization," in *Proc. IEEE Conf. Antenna Meas. Appl. (CAMA)*, Västerås, Sweden, Sep. 2018, pp. 1–4.
- [14] S. Srinivas and D. W. Bliss, "Conformal multi-service antenna arrays: Hybrid in situ & signal of opportunity (SoOP) calibration," in *Proc. IEEE 92nd Veh. Technol. Conf. (VTC-Fall)*, Victoria, BC, Canada, Nov. 2020, pp. 1–5.
- [15] R. M. Lebrón, P.-S. Tsai, J. M. Emmett, C. Fulton, and J. L. Salazar-Cerreno, "Validation and testing of initial and in-situ mutual coupling-based calibration of a dual-polarized active phased array antenna," *IEEE Access*, vol. 8, pp. 78315–78329, 2020.
- [16] C. Fulton, M. Yeary, D. Thompson, J. Lake, and A. Mitchell, "Digital phased arrays: Challenges and opportunities," *Proc. IEEE*, vol. 104, no. 3, pp. 487–503, Mar. 2016.
- [17] H. M. Aumann, A. J. Fenn, and F. G. Willwerth, "Phased array antenna calibration and pattern prediction using mutual coupling measurements," *IEEE Trans. Antennas Propag.*, vol. 37, no. 7, pp. 844–850, Jul. 1989.
- [18] D. Bekers, R. van Dijk, and F. van Vliet, "Mutual-coupling based phased-array calibration: A robust and versatile approach," in *Proc. IEEE Int. Symp. Phased Array Syst. Technol.*, Oct. 2013, pp. 630–637.
- [19] A. Agrawal and A. Jablon, "A calibration technique for active phased array antennas," in *Proc. IEEE Int. Symp. Phased Array Syst. Technol.*, Oct. 2003, pp. 223–228.
- [20] C. Fulton and W. Chappell, "Calibration techniques for digital phased arrays," in *Proc. IEEE Int. Conf. Microw., Commun., Antennas Electron.* Syst., Nov. 2009, pp. 1–10.



Adam C. Goad (Graduate Student Member, IEEE) received the B.S. degree in electrical and computer engineering from Baylor University, Waco, TX, USA, in 2019, where he is currently pursuing the M.S. and Ph.D. degrees.

His research interests include spectral coexistence techniques and real-time circuit optimization, especially for array-based joint radar communication, and 5G systems.



Austin Egbert (Member, IEEE) received the B.S., M.S., and Ph.D. degrees in electrical and computer engineering from Baylor University, Waco, TX, USA, in 2017 and 2021, respectively.

He is currently an Assistant Research Scientist with the Spectrum Management with Adaptive and Reconfigurable Technologies (SMART) Hub, Baylor University, developing deployable solutions for modern spectrum issues involving real-time circuit optimization and dynamic spectrum allocation.



Charles Baylis (Senior Member, IEEE) received the B.S., M.S., and Ph.D. degrees in electrical engineering from the University of South Florida, Tampa, FL, USA, in 2002, 2004, and 2007, respectively.

He is currently a Professor of electrical and computer engineering with Baylor University, Waco, TX, USA, where he directs the Wireless and Microwave Circuits and Systems (WMCS) Program. His research on spectrum issues in radar and communication systems has been sponsored by the National Science Foundation, the Army, and the

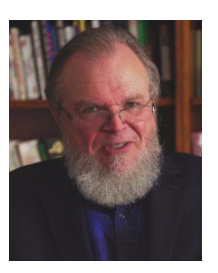
Navy. He has focused his work on the application of microwave circuit technology and measurements, combined with intelligent optimization algorithms, to create reconfigurable transmitters.

Dr. Baylis founded the annual Texas Symposium on Wireless and Microwave Circuits and Systems, where he serves as the Chair for the Executive Committee.



Trevor Van Hoosier (Graduate Student Member, IEEE) received the B.S. degree in electrical and computer engineering from Baylor University, Waco, TX, USA, in 2021, where he is currently pursuing the M.S. degree.

His research interests include spectral coexistence techniques and real-time circuit optimization for application to radar transmit amplifiers, and 5G systems.



Robert J. Marks II (Life Fellow, IEEE) is a Distinguished Professor of Electrical and Computer Engineering at Baylor University, Waco, TX, USA, and a Senior Fellow and the Director of the Walter Bradley Center for Natural and Artificial Intelligence, Seattle, WA, USA. He is the author of the book titled Non-Computable You: What You Do That Artificial Intelligence Never Will (Discovery Institute, 2022). He is the author of the books titled For a Greater Purpose: The Life and Legacy of Walter Bradley (Erasmus Press, 2020), Neural Smithing:

Supervised Learning in Feedforward Artificial Neural Networks (The MIT Press, 1999) and Introduction to Evolutionary Informatics (World Scientific, 2017).

Dr. Marks is a Fellow of Optica (formerly the Optical Society of America). His professional awards include the NASA Tech Brief Award and the IJCNN Pioneer in Neural Network Award. He is the Faculty Advisor of the Ratio Christi and American Scientific Affiliation Student Chapters at Baylor University. He has a Bacon-Erdős number of five. He is the Editor-in-Chief of BIO-Complexity and the former Editor-in-Chief of the IEEE TRANSACTIONS ON NEURAL NETWORKS AND LEARNING SYSTEMS.